The bathymetry of Moray Sinus at Titan's Kraken Mare

Valerio Poggiali, Alexander G. Hayes, Marco Mastrogiuseppe, Alice Le Gall, D. Lalich, I. Gomez-Leal, Jonathan Lunine

JGR Planets

RESEARCH ARTICLE

10.1029/2020JE006558

The Bathymetry of Moray Sinus at Titan's Kraken Mare

V. Poggiali[1], A. G. Hayes[1,2], M. Mastrogiuseppe[3], A. Le Gall[4,5], D. Lalich[1], I. Gómez-Leal[1], and J. I. Lunine[1,2]

[1]Cornell Center for Astrophysics and Planetary Science, Cornell University, Ithaca, NY, USA, [2]Astronomy Department, Cornell University, Ithaca, NY, USA, [3]Dipartimento di Ingegneria Dell'Informazione, Elettronica e Telecomunicazioni, Università di Roma La Sapienza, Rome, Italy, [4]LATMOS/IPSL, UVSQ Université Paris-Saclay, Sorbonne Université, CNRS, Paris, France, [5]Institut Universitaire de France (IUF), Paris, France

Abstract Moray Sinus is an estuary located at the northern end of Titan's Kraken Mare. The Cassini RADAR altimeter acquired three segments over this mare during the T104 flyby of Titan, on August 21, 2014. Herein, we present a detailed analysis of the received echoes. Some of these waveforms exhibit a reflection from the seafloor, from up to 85^{+28}_{-18} m of depth (1σ error). Monte Carlo simulations have been performed in order to assess the most probable values and estimation errors for the seafloor depth. Insights from this study, featuring the synergic use of the synthetic aperture radar images coupled to the altimetry and passive radiometry datasets, have been used to constrain the dielectric properties (i.e., absorptivity of the liquid) and roughness of this region of Kraken Mare. The resulting Ku-band specific attenuation of the liquid is 17^{+3}_{-3} dB/μs, corresponding to a loss tangent of $4.6^{+0.9}_{-0.9} \times 10^{-5}$, which is very similar to the loss tangent estimated at Ligeia Mare. The data in hand do not permit us to discern the most likely explanation for the lack of a seafloor reflection from the main body of Kraken Mare: either a very deep sea or a more absorbing liquid composition. However, if the main body of Kraken Mare is characterized by an absorption similar to Moray Sinus, then based on models of the response to altimetry mode observations we can conclude that it exceeds 100 m of depth, which is also compatible with radiometry observations.

Plain Language Summary From 2013 to 2017, we have been probing the depth of Titan's methane-dominated seas by penetrating the liquid with Cassini's radar altimeter. The depth and composition of each of the seas had already been derived, except for Titan's largest sea Kraken Mare. Herein, we describe the final observation of this campaign before the end of Cassini in 2017. Our analysis reveals that the seafloor at the center of Moray Sinus—an estuary located at the northern end of Kraken Mare, is up to 85 m deep. The radar waves are absorbed to an extent such that the liquid composition is compatible with 70% methane, 16% nitrogen, and 14% ethane (assuming ideal mixing). The analysis of the altimetry data in the main body of Kraken Mare showed no evidence for signal returns from the sea floor, suggesting the liquid is either too deep or too absorptive for Cassini's radio waves to penetrate. However, if the liquid in the main body of Kraken Mare is similar in composition to Moray Sinus, as one would expect, then its depth exceeds 100 m. This is compatible with a separate estimate using the radar as a "radiometer," sensing thermal energy from the sea at radio wavelengths.

Key Points:

- Moray Sinus is an estuary located at the northern end of Titan's Kraken Mare
- Analysis of Cassini's radar altimeter data shows that the near-shore local seafloor is up to 85 m deep in Moray Sinus estuary
- The composition of the sea, inferred from radar absorptivity, is very similar to that estimated at Ligeia Mare
- The main body of Kraken Mare exceeds 100 m of depth

Supporting Information:

- Supporting Information S1

Correspondence to:

V. Poggiali,
vpoggiali@astro.cornell.edu

Citation:

Poggiali, V., Hayes, A. G., Mastrogiuseppe, M., Le Gall, A., Lalich, D., Gómez-Leal, I., & Lunine, J. I. (2020). The bathymetry of moray sinus at Titan's Kraken Mare. *Journal of Geophysical Research: Planets*, *125*, e2020JE006558. https://doi.org/10.1029/2020JE006558

Received 7 JUN 2020
Accepted 5 NOV 2020

1. Introduction

Saturn's moon Titan is surrounded by a thick hazy atmosphere that is opaque to visible wavelengths. The lower troposphere is primarily composed of N_2 (94.2%), CH_4 (5.7%), and H_2 (0.1%) (Niemann et al., 2010). Operating in Ku-band (13.78 GHz), the Cassini RADAR instrument (Elachi et al., 2004) has been able to peer through Titan's atmospheric veil and confirm the presence of several liquid hydrocarbon lakes and seas (Stofan et al., 2007), mainly located in the Northern polar area (A. Hayes et al., 2008, 2017). The main scientific objective of the Cassini RADAR experiment was to carry out a first-order geological reconnaissance of Titan's surface and quantitatively characterize its properties (Elachi et al., 2004). During 13 years of Titan exploration (2004–2017), the radar operated in four different modes that were activated sequentially during the 127 Titan fly-bys. The radar produced maps of backscatter cross-section using its synthetic aperture radar (SAR) mode (Stiles, 2006), microwave thermal energy maps using its radiometer mode (Janssen et al., 2009, 2016), low-resolution backscatter maps using its scatterometer mode (West et al., 2009; Wye, 2011), and

topographical profiles of the surface using the altimeter mode (Alberti et al., 2007; Poggiali et al., 2019; Zebker et al., 2009).

In 2013 the SAR mapping campaign of the northern polar area of Titan was almost concluded when, during fly-by T91, the Cassini radar altimeter demonstrated its ability to probe the depth of Titan's seas by penetrating the low loss methane-dominated liquid. The possibility that this could be done was anticipated by Thompson and Squyres (1990) and Picardi (2008), but never built into the mission as a requirement. Ligeia Mare, the second largest sea of Titan, was determined to be ~170 m deep along the altimetric profile acquired during flyby T91 (Mastrogiuseppe et al., 2014). Following this initial discovery, a campaign to make similar observations of Titan's other liquid bodies was undertaken. The resulting data have been analyzed by Mastrogiuseppe et al. (2016, 2018a, 2018b, 2019b) to derive the liquid depth and composition. The fantastically transparent nature of the seas derived from the data led immediately to the presumption of liquid methane as an important or primary components of the seas, along with ethane and nitrogen as suggested by the nitrogen-dominated atmospheric composition and the phase behavior of the ternary mixture of methane, ethane, and nitrogen. When coupled with laboratory measurements of the complex dieletric constant of liquid hydrocarbon mixtures, these observations permitted the composition of each of the seas and lakes observed with altimetry to be predicted. Herein, we describe the final individual observation of that campaign to be published, the T104 flyby across Titan's largest sea Kraken Mare.

Stretching from 55°N to 82°N (Lorenz, 2014) and with a surface that covers 5×10^5 km^2 (A. G. Hayes et al., 2018b), Kraken Mare is the largest sea on Titan. During the T104 flyby (August 21, 2014), the Cassini spacecraft acquired altimetric data over three segments of its liquid surface (B, C, and D in Figure 1). Preliminary analysis of the data has shown no seafloor detection for the central and western parts of Kraken (Mastrogiuseppe et al., 2018a). Herein, we present an analysis of the radar altimeter echoes acquired over Moray Sinus, a bay located approximately at 77°N, 79°E in the northern part of Kraken Mare (basin D of Figure 1). Altimetry footprints collected over central Kraken were either saturated by the surface return or showed no evidence for returns from the sea floor, suggesting the sea was either too deep or too absorptive to penetrate or that the dielectric contrast between the liquid and the sea floor was very low (i.e., a negligible difference in their effective relative permittivity).

After a description of the datasets used for this study, we will show the bathymetry profile acquired at the end of the track over a much shallower part of the Kraken complex, Moray Sinus. Coupling the retrieved depths with the backscatter recorded in SAR mode over the same areas, we will describe how we estimated the attenuation and loss tangent of the liquid and found it to be similar to that of Ligeia Mare and Winnipeg Lacus. Using the inferred liquid composition, we will then incorporate the radiometry dataset acquired over Moray Sinus and the central Kraken portion of the track to provide lower limits to the depth for the central part of Kraken Mare. The results presented herein will be useful for computing a more complete carbon inventory for Titan and will facilitate a better understanding of the formation and evolution of its liquid bodies, as we discuss in the final section.

2. Dataset

The topography of the northern coasts of Kraken Mare, as shown by the height profiles in Figure 1 (central panel), is characterized by sudden drops of hundreds of meters, passing from solid to liquid surfaces (the threshold height tracker recorded up to >20° slopes over resolutions scales of <2 km). Four main basins (labeled A–D) are identified along the T104 altimetric profile. The first basin (A) extends from 80 to 140 km along track and it is ~300 m deep with respect to its surroundings. Its base shows discontinuous increases in backscatter in both the altimeter data and SAR images (Figure 1, upper panel, 67°N, 28°E). The smooth surface of this first basin (<5 m height standard deviation σ_h at tens of km scale) is characterized by a -0.7 ± 0.1 millidegrees mean slope along track and it is on average ~180 m higher than the liquid surface of Kraken Mare. If basin A is the relic of an ancient liquid-filled gulf of Kraken Mare, the relatively flat topography of its floor could be an interesting analog for Kraken seafloor characteristics. About 170 km of solid surface separates basin A from basin B (or Arnar Sinus), where the Kraken liquid body extends for ~100 km along track interrupted only by the presence of a small promontory at ~350 km from the beginning of the T104 track. Similar to what happened during the Ontario Lacus observation (fly-by T49; Mastrogiuseppe

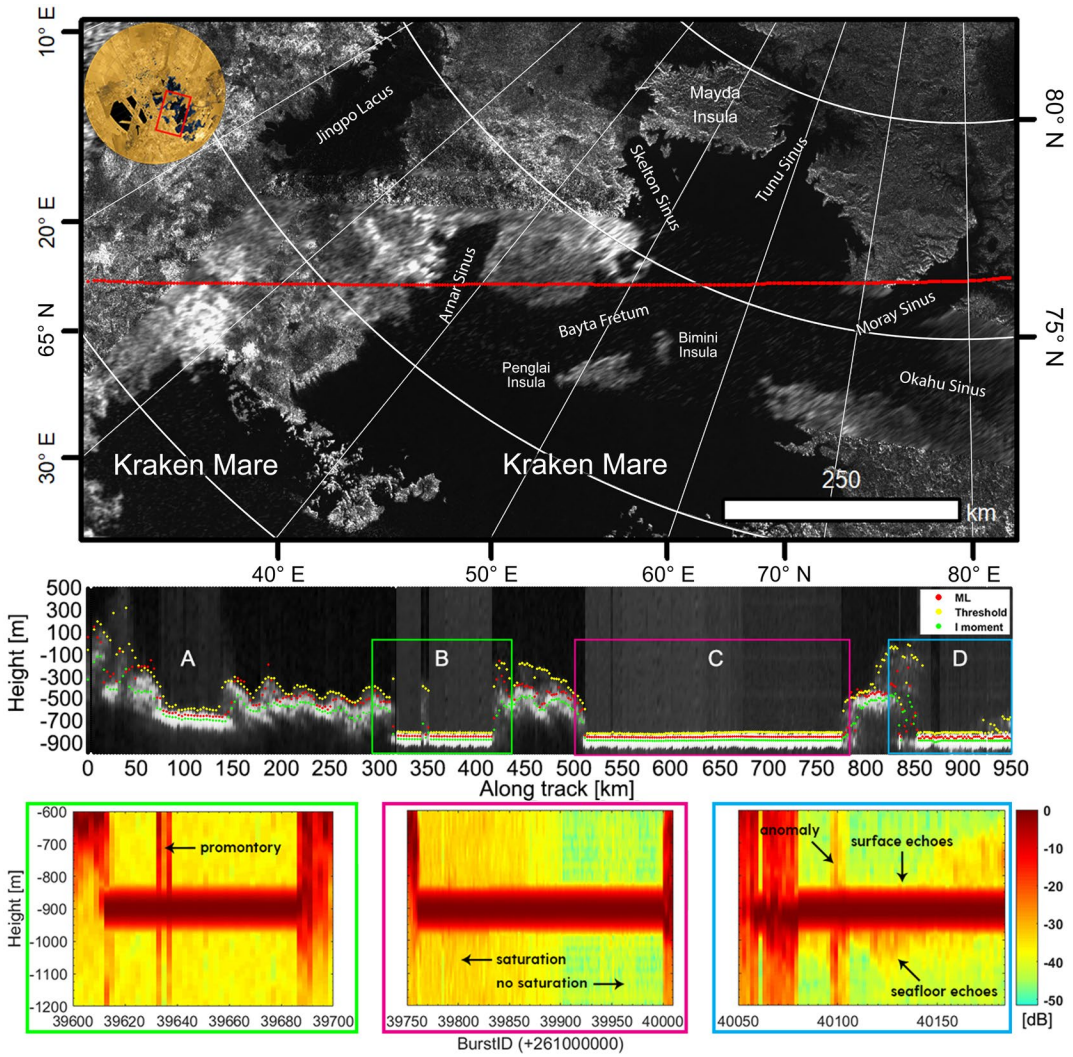

Figure 1. SAR mosaic of the northern region of Kraken Mare with the T104 fly-by altimetry ground track in red: the map is in Polar Stereographic projection with the North Pole approximately toward the upper right (above). Altimetry profile with highlighted positions of the three sections where the footprint intercepted the liquid surface of Kraken Mare. The central and upper panels have the same horizontal coordinate (center). Normalized received power radargrams showing the lack of seafloor reflections from the main liquid body of Kraken mare (basins B and C) in contrast with Moray Sinus (basin D), where multiple waveforms show a shallow signal return from the seafloor (below). SAR, synthetic aperture radar.

et al., 2018a; L. C. Wye et al., 2009), the strong reflection received from the extremely flat sea surface caused the radar receiver to saturate with the consequent clipping of the received chirped signals (Figure S1). The strong saturation of the received echoes prevents the reconstruction of the actual values of radar cross section (RCS) and backscatter of the main portions of Kraken Mare (basins B and first part of C), before ~710 km along track. We have selected only the echoes received from the last part of the main body of Kraken Mare and from Moray Sinus (respectively the last part of basin C and basin D), where saturation is not present or moderate (<1%); the first two rows of Table 1 and Figure S1 display the measured values of backscatter (obtained after scaling the RCS over the −3 dB beam-limited footprint and correcting off-nadir angle and planetary curvature effects).

While the altimetric radargram acquired on Moray Sinus covers ~100 km of ground track and includes multiple waveforms that exhibit shallow reflections from the seafloor, there is no evidence of any signal in addition to the echo received from the surface of the main body of Kraken Mare (compare radargrams B

Table 1
Name of the Mare; Average Spacecraft Altitude Over the Area of Measurements; Number of Unsaturated Bursts Used for the Measurements; Average Latitude and Longitude of the Area of Measurements; Average Radar Cross Section (RCS) Estimated From Unsaturated Bursts; Average Backscatter Estimated From Unsaturated Bursts; Standard Deviation of the Backscatter Estimated From Unsaturated Bursts

Mare	SC alt (km)	*N* bursts	LAT (°)	LON (E°)	RCS (dB)	Backscatter (dB)	Backscatter STD (dB)
Kraken (basin C)	2,700	31	75.9	65.3	101.6	24.4	0.4
Kraken (Moray Sinus)	3,150	34	76.3	80.3	102	24.2	1.3
Ligeia (South)	1,500	21	78.5	61.3	107.4	32.9	0.5
Ligeia (North)	1,700	17	81.4	62.1	106.8	31.9	0.9
Punga	1,100	25	84.2	132.1	102.1	29.5	0.7

Note. RCS increases as the illuminated area increases; thus for surface studies we use the backscatter coefficient, whose values are obtained from the RCS by normalizing the −3 dB beam limited area of the footprint and correcting for antenna mispointing effects and the planet curvature (RT = 2,575 km). The area of Moray Sinus where the received power anomalous drop has been recorded (869–876 km along track) has been also filtered out. As a reference, although backscatter on Titan shows a wide range of variation even for the same class of surface features, as a rule of thumb it spans approximately over dune fields between 5 and 15 dB and on mountains it lies between 0 and 10 dB. Note that the difference in backscatter of level solid surfaces composed respectively of pure water and methane ices is about 6.7 dB, with actual absolute values varying with surface roughness.

and C with respect to radargram D in Figure 1). The seafloor reflections in Moray Sinus appear as echoes delayed in time with respect to the strong reflection from the sea surface (see the black arrows in the lower-right panel of Figure 1). Their presence is evident after applying standard processing routines (Alberti et al., 2007) but, in order to enhance their detectability we applied the super resolution technique proposed by Mastrogiuseppe et al. (2014) and described in detail by Raguso et al. (2018). This technique is able to increase the standard resolution of the Cassini radar altimeter (35 m) up to three times and produce the super resolved radargram shown in Figure 2 (panel a). This radargram has been normalized with respect to the most powerful echo received from the sea surface in order to allow visualization of the actual small variations in surface received power. The presence of seafloor echoes in the altimetric data is also consistent with the fact that some signal from the seafloor was already present in the T28 SAR image of the area as a slight but progressive increase of brightness along the altimetric track (see Figure 2, panel c).

In the radargram of Figure 2 (panel a), we note the presence at ∼77°E longitude (around the BurstID 261040100) of an anomalous decrease in the signal received from the sea surface of about 22 dB. A. G. Hayes et al. (2011) described significant differences in backscatter (up to ∼11 dB) between two SAR images (T25 and T28) available in this area and its surroundings (see Figure 2, panels c and d). These images were acquired in 2007 over Moray Sinus, about 6 weeks apart and with similar observation geometries. The difference in backscatter was ascribed to the possible presence of a transient surface layer with distinct dielectric properties, such as a layer of suspended or floating organic debris that sunk or dispersed by the time of the T28 observation (A. G. Hayes et al. 2011). Seven years later, at the time of the T104 observation in 2014, this estuary-like area still showed apparent indications of activity, perhaps connected to the nearby presence of the big drainage network extending from Kraken in the direction of Ligeia Mare. Due to the uncertainty regarding the cause of this anomaly, we exclude this region from our analysis; it is briefly described in A. G. Hayes et al. (2018a) and will be considered in a detail in a forthcoming manuscript.

The radar altimeter uses the 4-m diameter nadir-pointed Cassini's parabolic antenna to transmit bursts of 21 chirped signals, 15 of which are typically received back and incoherently integrated in order to improve signal-to-noise ratio (SNR) and to reduce speckle noise effects. At the spacecraft altitude from which this observation was acquired (∼3,150 km) the modality of observation of the Cassini radar altimeter was beam-limited (9.7 km average radius −3 dB footprint). This reduces the possibility of receiving lateral clutter echoes from the coasts located in the cross-track direction (i.e., at the center of the bay the antenna pattern will attenuate such signals up to about −35 dB). Also, in order to exclude the possibility of receiving along-track lateral clutter from coastlines and/or from the anomaly at the same time delay of the seafloor

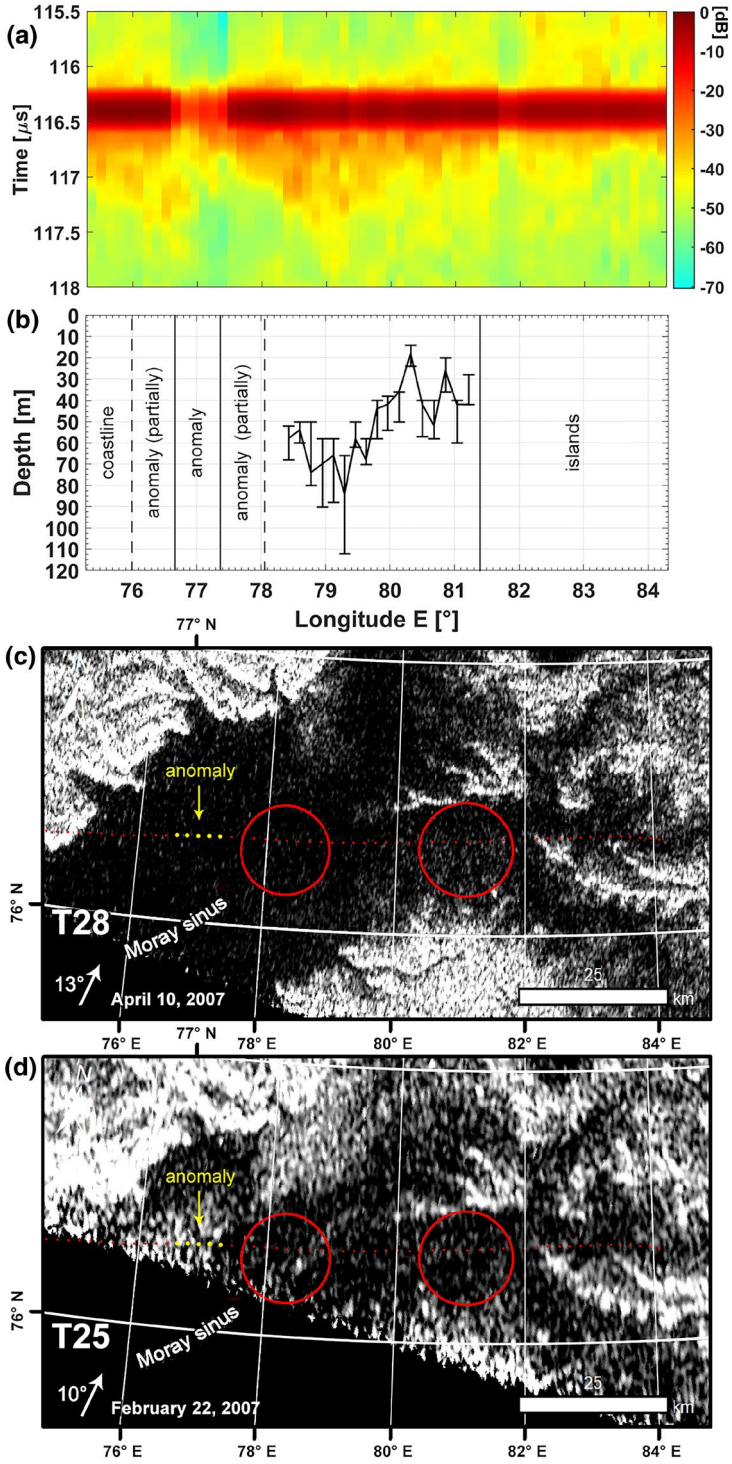

Figure 2. (a) Super resolution enhances the detectability of the echoes received from the seafloor of Moray Sinus. Here the radargram is normalized with respect to the most powerful echo received from sea surface in order to account for the small variations in the surface received power and the anomalous sudden drop of ~22 dB recorded at about 77°E longitude. (b) Estimated bathymetry with associated 1σ error bars; (c) T28 SAR image acquired over Moray Sinus on April 10, 2007; (d) T25 SAR image acquired over Moray Sinus on February 22, 2007. Note that T25 has a lower resolution than the T28 SAR image. The red circles and dots in panels (c) and (d) indicate respectively the contour of −3 dB antenna footprint at the extremes of the bathymetry track and all the footprint centers of the T104 altimetric observation of Titan relative to the area of Moray Sinus (August 21, 2014). SAR, synthetic aperture radar.

echoes, we have coherently reprocessed the T104 altimetric data by averaging only the three central filters at nadir (each one of them associated with a ∼3.2 km Doppler footprint along-track). Then, we have compared the resulting radargram with the one obtained through incoherent processing (Figure S2). Since the delayed echoes are present in both radargrams, they can be most likely recognized as seafloor nadir reflections.

The nearby presence of the coasts and the anomaly (at ∼77°E) requires a careful selection of those echoes that are suitable for depth and liquid composition analysis. In particular, our depth estimation method uses the T104 incoherently averaged echoes representing the signal reflected from the −3 dB beam-limited footprints. Given that there is ∼1.8 km separation between consecutive footprints it becomes clear that, in order to consider only footprints completely and solely illuminating a liquid surface, we will be forced to exclude from our study the seven echoes located between the coast and the anomaly and the first five echoes after the anomaly itself (9.7/1.8 km ≅ 5.4, see panels c and d of Figure 2).

The T104 radiometry dataset acquired at nadir will also be used for our study. The microwave nadir emissivity values are accurate to about 1%, but the relative precision within individual data sets can be at least twice smaller (Le Gall et al., 2016). Emissivity values have been obtained by dividing the measured brightness temperatures by the physical temperature, using the model described in Janssen et al. (2016), which accounts for variations with time and latitude.

3. Method and Results

We performed a Monte Carlo waveform simulation and adopted a least squares estimation fitting approach to retrieve values of seafloor depth as described in Mastrogiuseppe et al. (2016), where it is shown that the waveforms received from the liquid bodies of Titan can be accurately described by a two-layer model accounting for the three input parameters P_S/P_{SS} (surface vs. seafloor echo power ratio), τ (two-way travel time indicative of the seafloor depth) and m (seafloor footprint-scale roughness). In order to make a robust determination of depth values together with their associated estimation errors, we have compiled a lookup table of simulated radar echoes covering the widest possible range of values for the three parameters of interest. We explored the complete range of bathymetric depths from 0.1 to 2.2 μs at 0.02 μs steps (i.e., 10–250 m at 2 m steps, with a dielectric constant of the liquid of 1.7). We have also varied the P_S/P_{SS} from 10 dB to 45 at 1 dB steps and the seafloor footprint-scale roughness from 0 to 44 m at 2 m steps. This wide range of simulations resulted in $\sim 10^5$ combinations of model parameters. Then, we have produced 400 Monte Carlo realizations of each parameter triplet of the model parameters accounting for the thermal noise amplitude measured during the T104 Moray Sinus observation. Each Monte Carlo realization provides a waveform characterized by distinct speckle and thermal noise characteristics. Using a least-square estimation fitting of each received waveform to the set of simulated echoes, we have determined the best fit triplet of model parameters and the associated probability density functions for each seafloor echo that has been analyzed. The panel b of Figure 2 shows the maximum *a posteriori* probability values for the depth of Moray Sinus (limited to the 17 echoes that were suitable for analysis) with their associated confidence intervals at 1-sigma (note that the width of the error bars depends mainly on the SNR of the subsurface echoes and on the seafloor roughness).

Along the section of the T104 altimetric track that was suitable for seafloor depth estimation (bounded by the two footprints shown in Figure 2, roughly from 78.4°E to 81.2°E), Moray Sinus appears to be an estuary-like morphologic feature with a maximum depth of 85^{+28}_{-18} m and an average depth of ∼50 m. The deepest point is located at the center of the bay, at about 79.3°E, where the T28 SAR image appears darker (see Figure 2, panel c). We avoid to perform any bathymetric estimation before 78.4°E, because of the proximity of the coast and the presence of the surface anomaly. The bathymetric profile stops at 81.2°E longitude due to the shallowness of the sea (<∼15/20 m) and to the presence of islands.

In Figure 3, we show an example of two altimetric echoes, acquired during flyby T104 over Moray Sinus, where the peak of a shallow seafloor echo is clearly apparent slightly delayed and strongly attenuated with respect to the sea surface echo.

Both the limited number of independent seafloor depth measurements (consecutive footprints are largely superimposed on each other) and the short range of variation of the bathymetry make the estima-

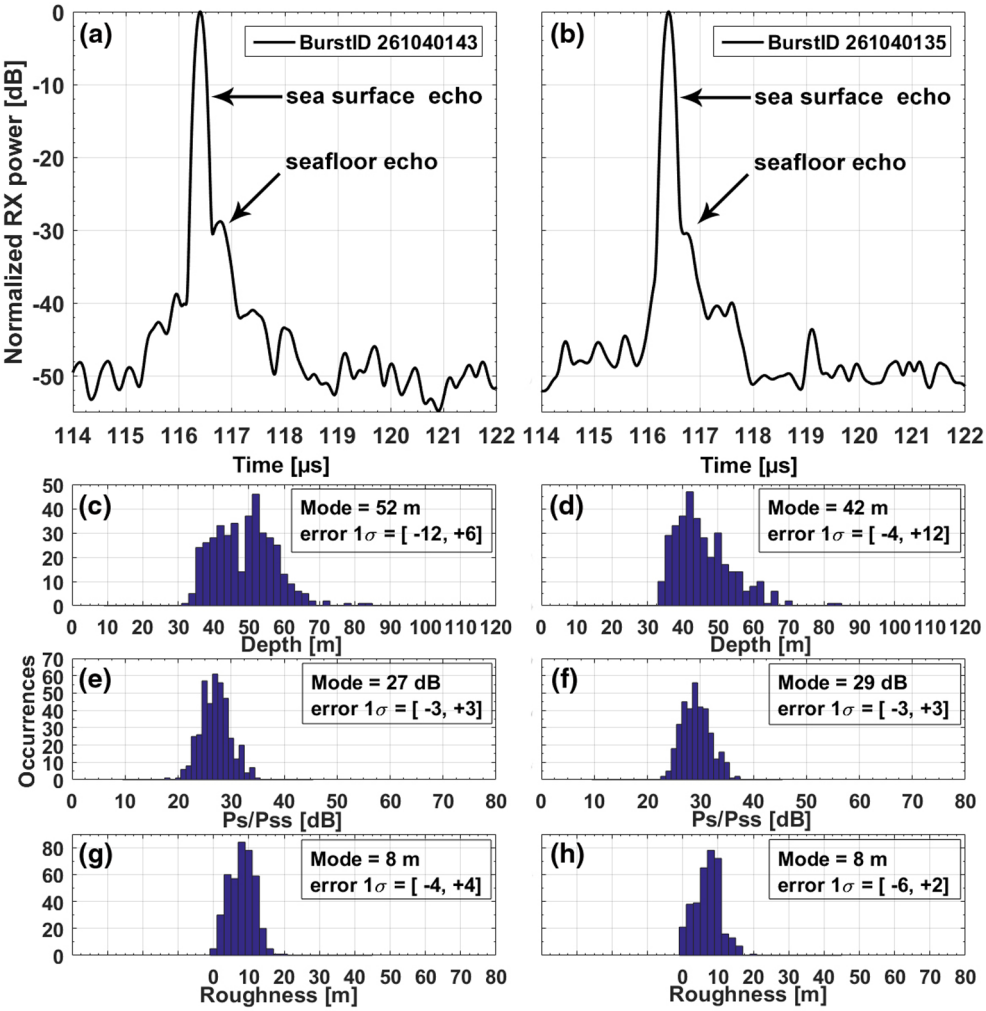

Figure 3. Two altimetric echoes returned from the shallower coastal area of Moray Sinus (BurstID 261040135 at 79.96°E and BurstID 261040143 at 80.68°E). These echoes have been obtained by means of incoherent processing and application of the superresolution algorithm (upper panels). Posteriori probability distributions of the estimated parameters of interest (depth, Ps/Pss and footprint-scale roughness) obtained for the echoes shown in the upper panels (lower panels). For the convenience of the reader, we plotted the depth's distribution as obtained from a permittivity of the liquid of 1.7 (value also inferred from cryogenic liquid alkanes mixture models [Born & Wolf, 1999] and laboratory measurements [Mitchell et al., 2015] as well as from passive radiometry [Le Gall et al., 2016)].

tion of the liquid medium attenuation a prohibitive task that cannot be tackled with the techniques described by Mastrogiuseppe et al. (2016) as the result would eventually show a 50% error. However, supposing that the liquid is relatively uniform with time (i.e., it has the same dielectric properties and scattering losses along the region of interest between flybys), it is possible to use the available SAR images of the area in connection with the depths given by the altimeter to get a more accurate estimate of the attenuation.

Using the values of RCS (see Table 1) obtained for the altimetric sea surface echo on Moray Sinus and applying the Physical Optics (PO) model (Picardi et al., 2008; Zebker et al., 2014) with a permittivity value of the liquid surface of $\varepsilon_s = 1.7$ (inferred from cryogenic liquid alkanes mixture models [Born & Wolf, 1999] and laboratory measurements (Mitchell et al., 2015) as well as from passive radiometry [Le Gall et al., 2016]), we retrieve an average sea surface small-scale roughness characterized by a root mean square (RMS) height σ_h of 2.4 ± 0.1 mm. Note that we can apply the PO model because the received sea surface echoes look

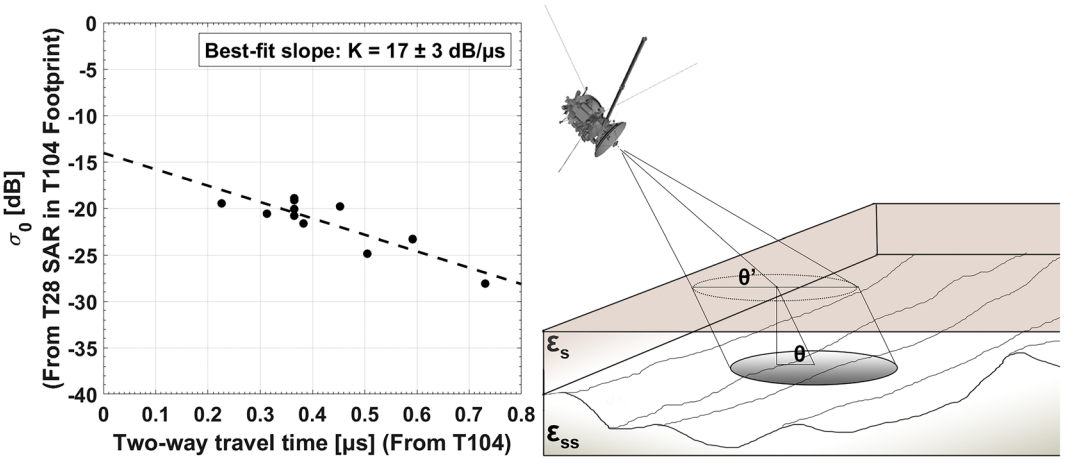

Figure 4. T28 SAR average backscatter versus two-way travel time between the first and the second reflection as determined by analysis of the T104 radar altimeter dataset (left panel). The standard deviation on the backscatter obtained by averaging SAR backscatter over each area is very small (<<1 dB) and almost constant for every data value used for the fitting. Geometry of the observation: θ' and θ are respectively the off-nadir angle of the Cassini antenna and the incidence angle of the signal at the seafloor, ε_S and ε_{SS} are respectively the permittivity of the liquid medium and the seafloor (right panel). SAR, synthetic aperture radar.

like a scaled version of the transmitted chirped signals (see Figure S1) and their RCS is >300 times (25 dB) brighter that the land echoes and, thus, we can affirm with confidence that the signal reflected back at the radar from the surface of the sea is mainly coherent in nature. The value that we found satisfies the Rayleigh criterion ($\sigma_h < \lambda/8$) for a surface to be considered smooth at the Cassini wavelength ($\lambda = 2.17$ cm). We calculate the Ku-signal absorption properties of the liquid by performing a linear regression of the SAR backscatter (σ_0) (averaged over consecutive and not superimposing rectangular areas) versus the two-way travel time τ, obtained at each of those locations by the radar altimeter. (The result is the same whether or not the SAR-backscatter is weighted with the antenna pattern.) We have used a two-layer model (A. G. Hayes, 2016; Hayes et al, 2010, 2011, 2014) to describe behavior of the SAR backscatter $\sigma_0 = \sigma_S + \sigma_{SS} e^{-8\pi k d \sec\theta/\lambda}$, where θ and σ_{SS} are the incidence angle and backscatter at the seafloor, respectively, and k and σ_S are the imaginary component of the liquid's index of refraction and the backscatter at the sea surface (negligible in an off-nadir geometry), respectively.

Unlike nadir looking geometries, SAR backscatter values generally need to be corrected for the incidence angle θ' at the sea surface or, in this case, the refraction angle θ inside the liquid medium (which is equal to the final incidence angle of the signal at the seafloor). Note that the one-way travel path for the signal through the liquid medium is thus equal to $d * \sec(\theta)$, with $\theta = \sin^{-1}(\sin(\theta') / \sqrt{\varepsilon_s})$ obtained from Snell's law, and ε_s the relative dielectric constant of the liquid layer (see the model scenario in Figure 4). However, the T28 SAR image of the study area presents a very limited range of incidence angle θ' variation (between 12.6° and 13°). Thus, independently from the composition of the liquid hydrocarbon mixture filling the sea, the path length will vary only <7 cm along the bathymetry track and the correction becomes practically unnecessary. Figure 4 shows the result of the linear regression applied to SAR pixels selected on the T28 SAR image. The Ku-band specific attenuation of the liquid (slope of the line) obtained is equal to $K = 17 \pm 3$ dB/μs (or 0.15 ± 0.03 dB/m, assuming $\varepsilon_s = 1.7$). Note that for this estimation we selected only the depths relative to the eastern half of the bathymetric profile (the coastal area of Moray Sinus). This is motivated by the fact that the SAR backscatter approaches the noise floor for most of the deeper measurements. On the other hand, a similar (but less reliable) result can be obtained with the other available SAR image of the area (from flyby T25). The estimation error in that case is twice the value obtained for the T28 flyby due to the anomalous variations in backscatter recorded in the area at the time of the T25 flyby (A. G. Hayes et al., 2011). The estimated specific attenuation can be converted into loss tangent of the liquid (ratio between the imaginary and the real parts of the permittivity) by means of the formula $\tan\Delta = K/(27 f_0)$, where f_0 is the Cassini radar carrier frequency expressed in MHz (Picardi et al., 2008; Mastrogiuseppe

Table 2
Name of the Liquid Body; Specific Attenuation in (dB/μs); Specific Attenuation in (dB/m) in the Hypothesis That the Permittivity of the Liquid Medium is $\varepsilon_s = 1.7$; Loss Tangent; Composition (in Volume Fraction) of Titan Liquid Bodies Assuming a Ternary Methane-Ethane-Nitrogen Mixture; Latitudinal Extension of the Liquid Body

Liquid body	K (dB/μs)	K (dB/m) ($\varepsilon_s = 1.7$)	tanΔ ($\times 10^{-5}$)	CH_4 (%)	C_2H_6 (%)	N_2 (%)	Latitude (°)
Baffin Sinus[a]	10 (−8, +6)	0.08 (−0.07, +0.05)	3 (−2, +1)	80(74–80)	20(18–20)	0 (0–8)	~80–81°N
Punga Mare[a]	13 (−6, +5)	0.11 (−0.05, +0.04)	3 (−1, +1)	80(74–80)	20(18–20)	0 (0–8)	~83–87°N
Ligeia Mare[b]	16 (−4, +4)	0.14 (−0.03, +0.03)	4.4 (−0.9, +0.9)	71(63–78)	12 (2–23)	17(14–20)	~75–83°N
Winnipeg Lacus[c]	17 (−7, +7)	0.15 (−0.06, +0.06)	4.6 (−1.8, +1.8)	69(54–80)	15 (0–3 5)	16(11–20)	~78°N
Moray Sinus	17 (−3, +3)	0.15 (−0.03, +0.03)	4.6 (−0.9, +0.9)	70(62–77)	14 (4–24)	16(14–19)	~76–79°N
Ontario Lacus[d]	22 (−10, +10)	0.2 (−0.09, +0.09)	6 (−3, +3)	57(30–80)	31 (0–64)	12 (6–20)	~71–74°S

Note. The values reported in this table are indicated with their relative 1σ errors and can be found in the papers as indicated below.
[a]Mastrogiuseppe et al. (2018b). [b]Mastrogiuseppe et al. (2016). [c]Mastrogiuseppe et al. (2019b). [d]Mastrogiuseppe et al. (2018a).

et al., 2016). This results in a loss tangent equal to $4.6^{+0.9}_{-0.9} \times 10^{-5}$. The value obtained is very similar to the one found at Ligeia Mare and Winnipeg Lacus (see Table 2). Under the assumption that the liquid composing the seas and lakes is a ternary mixture of methane, ethane, and nitrogen under Titan atmospheric conditions, using the N_2 solubility data in Malaska et al. (2017) and assuming the Lorentz-Lorenz relation (Born & Wolf, 1999), this value of loss tangent corresponds to a volumetric composition of 70 (62–77)% CH_4, 16 (14–19)% N_2, and 14 (4–24)% C_2H_6 (range in parenthesis corresponds to 1 − sigma errors). The permittivity of such a mixture would therefore be equal to 1.7. The similarity between the compositions of Ligeia and Kraken Mare at Moray Sinus may be explained by the connection between these two bodies at the Trevize Fretum and possibly through the channels of which Moray Sinus represents the terminus (see Figure S3). Subsurface connectivity through a porous polar regolith is also a possibility (A. Hayes et al. 2008).

Using the PO formulation and the T104 altimetric values of RCS, we previously retrieved a useful estimation of the sea surface average small-scale roughness in terms of RMS height σ_h. Now, by means of the Geometrical Optics model (Ulaby et al., 1982), we can investigate the seabed average small-scale roughness (f_{SS}), expressed as the average RMS geometric slope m. In the absence of volume scattering, the signal extinction depends solely on the absorption of the liquid medium varying the length of the two-way travel time τ. The dielectric contrast at the interface between the liquid and the seabed also plays a fundamental role by varying the magnitude ratio between the surface and subsurface echoes (P_S/P_{SS}) previously determined. Thus, in the case of having nadir observations and parallel interfaces, the Fresnel subsurface reflectivity Γ_{SS} can be expressed by means of the inversion formula (Picardi et al., 2008):

$$\Gamma_{SS}\big|_{dB} = \Gamma_S\big|_{dB} - \left(1-\Gamma_S\right)^2\big|_{dB} + \left(K\cdot\tau\right)\big|_{dB} + \frac{f_S}{f_{SS}}\Big|_{dB} - \frac{P_S}{P_{SS}}\Big|_{dB} \quad (1)$$

where the indexes S and SS indicate respectively the surface and subsurface related parameters and Γ_S is the Fresnel surface reflectivity. Note that the subsurface reflectivity Γ_{SS} can also be expressed as a function of surface permittivity ε_S and subsurface permittivity ε_{SS}

$$\Gamma_{SS} = \left|\frac{\sqrt{\varepsilon_{SS}} - \sqrt{\varepsilon_S}}{\sqrt{\varepsilon_{SS}} + \sqrt{\varepsilon_S}}\right|^2 \quad (2)$$

and therefore, the subsurface permittivity itself can be expressed as

$$\varepsilon_{SS} = \varepsilon_S\left(\frac{1+\sqrt{\Gamma_{SS}}}{1-\sqrt{\Gamma_{SS}}}\right)^2 \quad (3)$$

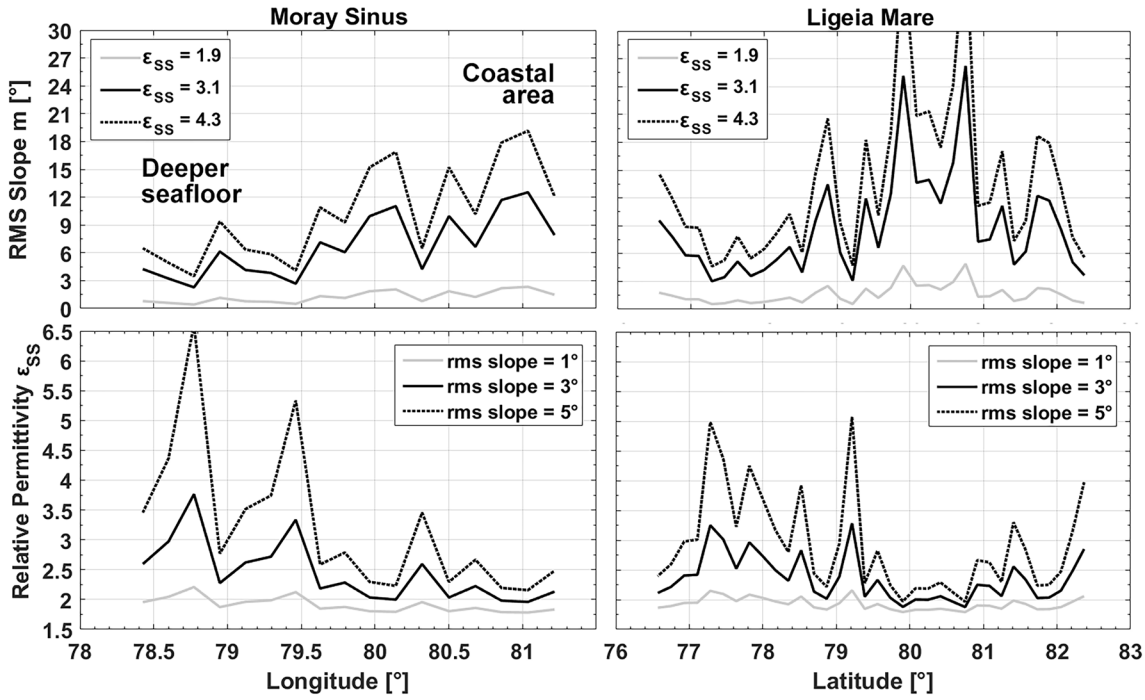

Figure 5. Comparison between the values of permittivity and seafloor small-scale roughness estimated for the deeper and shallower portions of the seafloor at Moray Sinus and Ligeia Mare. Note that the lower-right panel is the same shown also in Mastrogiuseppe et al. (2018b).

Using Equation 1, we have investigated the characteristics of the coastal and deep seafloor at Moray Sinus along the T104 track. Later, we have compared them to the northern and southern seafloor regions of Ligeia Mare by making the hypothesis of having similar sea state conditions at the surface (f_S) and making use of the already estimated specific attenuation K of Moray sinus and Ligeia mare, that have been found to be 17 and 16 dB/μs, respectively. In Mastrogiuseppe et al. (2016), we noted that the echoes acquired in the northern area of the Ligeia's seafloor presented a shape that is indicative of a larger seafloor roughness at the radar footprint scale. This is also confirmed by SAR imaging, which shows significant backscatter variations at the 300-m pixel scale that are likely from the seafloor. In northern Ligeia, the Xanthus Flumen fluvial system is likely depositing material on the seabed of Puget Sinus that is contributing to the observed roughness (Mastrogiuseppe et al., 2016). The stability of the sea surface nadir backscatter measured by the radar altimeter along the track for both Ligeia Mare and Moray Sinus (STD $\leq \sim$1 dB, see Table 1 and Figure S1) is indicative of relatively homogeneous composition and small-scale roughness at the surface of the two seas. Therefore, the observed variations of P_s/P_{SS} along the altimetric track can be ascribed to variations in the seafloor permittivity, its small-scale roughness, the permittivity of the liquid medium beneath the surface of the sea, or all three in combination. Despite the limitations of the T104 altimetric dataset (e.g., the high degree of superimposition between consecutive footprints) we can use the P_S/P_{SS} ratio obtained along the tracks of Ligeia Mare and Moray Sinus to compare their seafloors. For this purpose, we arbitrarily assumed three values for the subsurface scattering term (f_{SS} = {1°, 3°, 5°} of RMS slope) and three values of the seafloor permittivity (ε_{SS}={1.9, 3.1, 4.3}) and we assumed the permittivity of the overlying liquid medium to be homogenous. Note that despite being arbitrary, the values adopted are plausible for Titan.

The result of the comparison is shown in Figure 5. If we divide the estimated values within two groups (i.e., the echoes at greater depth—78.5°E–79.5°E and the shallower ones closer to the coast—79.5°E–81°E) and average them, we note a clear distinction. This result indicates a lower value of the permittivity for the coastal seafloor of Moray Sinus with respect to its deeper portion and/or a higher value of the seafloor small-scale roughness close to the coast (see Figures 5 and S4). While absolute estimations of these parameters are not possible because of their interdependency, it is interesting to note that the seafloor adjacent to the coastal

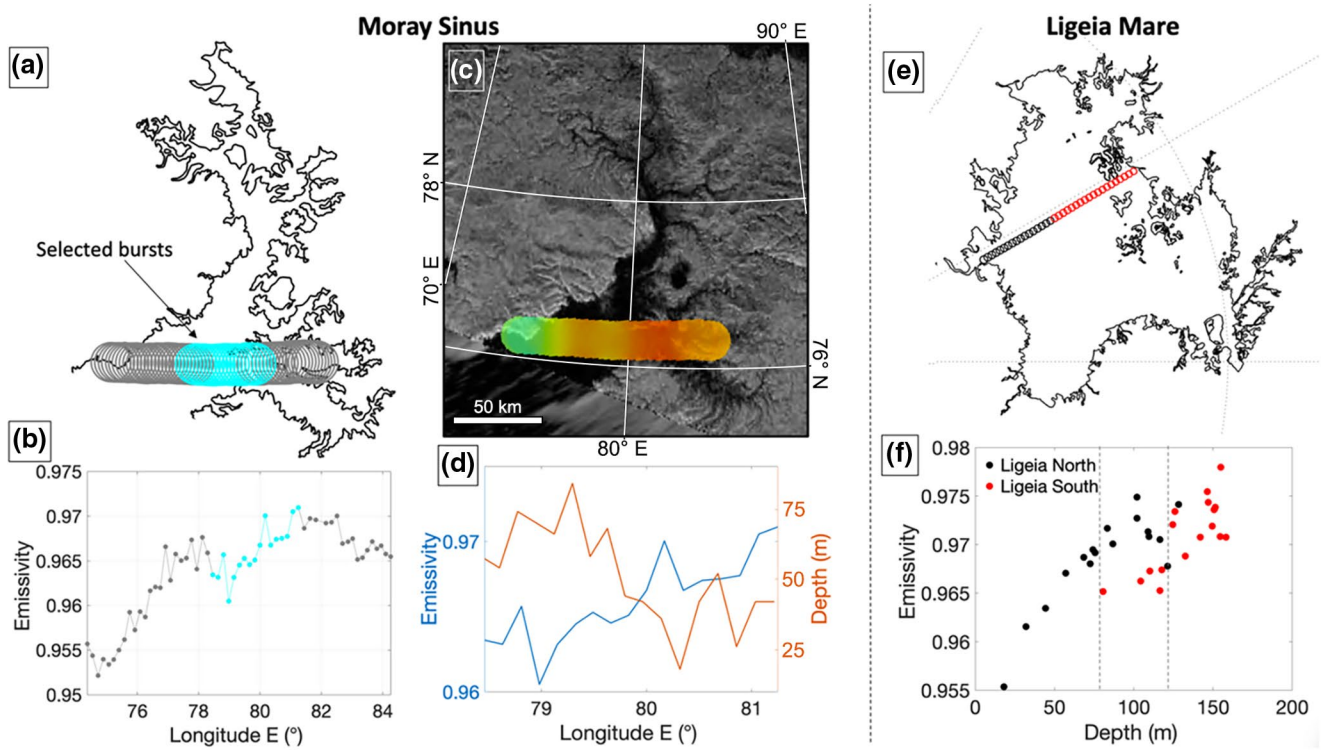

Figure 6. Left and middle: Radiometric footprints in the last section of the T104 altimetry track over (a) Moray Sinus and (b) associated measured emissivities. The footprints of interest and their emissivity values are in cyan. (c) After a decrease in emissivity starting around 72°E due to the presence of the solid surface of the promontory, we note a gradual increase over Moray Sinus as also shown on the radiometry map overlaid on a SAR mosaic. The transition is gradual because of the low resolution of the radiometry dataset (footprint of ~25 km diameter). (d) The comparison between the altimetric depth and the radiometric emissivity; we note an anticorrelation. Right: (e) The radiometry footprints over Ligeia Mare during the T91 altimetry observation; the northern footprints are in black, the southern ones in red. (f) The comparison between the emissivity recorded in the northern and southern portions of Ligeia Mare versus the depth of the seafloor. At equal depth the southern portion shows a lower emissivity. SAR, synthetic aperture radar.

portion of Moray Sinus behaves similarly to the northern region of Ligeia Mare—79.5°N–82°N and fluvial systems flow into both of them (see map in Figure S3).

This is also consistent with the behavior of the microwave nadir emissivity. The T104 radiometric dataset over Moray Sinus, acquired nearly simultaneously with the altimetry dataset (radiometry observations are interspersed between active footprints), observed microwave nadir emissivity values between 0.96 and 0.97 (Figure 6, panels a and b). Unfortunately, the precision (<0.3%) of the emissivity values for this dataset is not large enough relative to footprint-to-footprint variations to allow a thorough analysis. However, we do note that the emissivity increases as the footprint approaches shallower seafloors (Figure 6, panels c and d). This behavior is unexpected; the emissivity should decrease as the contribution from the seafloor increases (mainly because of the seafloor's larger dielectric constant which implies a smaller emissivity [Le Gall et al., 2016]). Considering again the likely sea surface homogeneity in terms of composition and small-scale roughness, the emissivity variations near the shore may be the result of a smaller seafloor permittivity, a larger small-scale roughness, a liquid permittivity smaller than in the deeper central part of Moray Sinus, or all three. Figure 7 presents a scenario where the liquid permittivity decreases and the seafloor roughness increases close to the coast due to the injection of materials coming from a nearby river. Interestingly, a similar difference in the emissivity values has been observed between the northern and southern portions of the seafloor in Ligeia Mare (Figure 6, panels e and f), where the emissivity values recorded at similar depths over the two areas are substantially higher in the northern portion. Note that increases of emissivity found at the mouth of rivers is also a common phenomenon on our own planet, that is the injection of Amazon river freshwater extending for tens of kilometers into the saltier Atlantic Ocean (see Figure S5 [Fournier

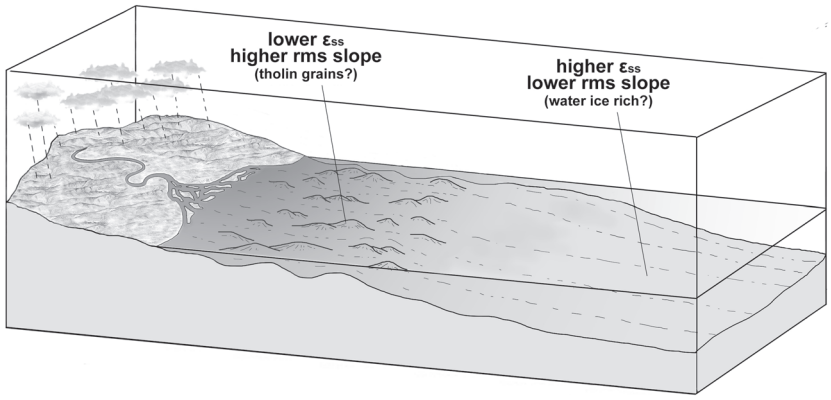

Figure 7. Model scenario of a river culminating in a liquid body. The flow deposits larger-dimension particulates close to the river terminus while more distant seafloor areas remain unaffected.

et al., 2015]). This result is also compatible with the slightly lower nadir backscatter recorded at the sea surface of the northern portion of Ligeia ($31.9^{+0.9}_{-0.9}$ dB) relative to its southern portion ($32.9^{+0.5}_{-0.5}$ dB, see Table 1).

4. Depth Limits for the Central Portions of Kraken Mare

For the western and central portions of Kraken Mare (basins B and C), we reprocessed and analyzed the received altimetric echoes both with incoherent and coherent processing and found a total lack of both secondary reflections from the sea floor as well as volume scattering (i.e., no enlargements in the trailing-edge of the sea surface echo), indicating that the medium is devoid of observable suspended particles at 2.17 cm wavelength. This is also consistent with the total lack of signal and noise level variation in the T28 SAR image of the basin C. The power reflected at the radar is exclusively coming from the sea surface and shows an average SNR of about ∼47 ± 0.6 dB (for this measurement only the unsaturated data from basin C has been used). The capability of the radar to receive a reflection from the sea floor at a given depth of liquid varies with the composition and roughness of the surface and seafloor, as well as the dielectric properties of the liquid medium. Using Equation 1 and considering the recorded value of SNR, we can infer what would have been the magnitude of the received seabed echo and the minimal depth for the central portion of Kraken Mare (basin C) in order for it to be at least distinguishable from the random variations of the noise (i.e., SNR ≥ 5 dB), in the assumed case of a sea surface state and liquid medium on average similar to those found at Moray Sinus. This assumption is justified by two facts: first, basin C and Moray Sinus are adjacent sea areas located at about the same latitude and only partially separated by the geographical barrier represented by a promontory; second, the unsaturated surface backscatter recorded in the last part of the basin C and on Moray sinus are similar within the 1-sigma uncertainty of the estimates (24.4 ± 0.4 and 24.2 ± 1.3 dB, respectively) suggesting that the two regions of the sea may also be similar in liquid composition and both characterized by a quite smooth surface (the reflectivities of pure methane and ethane differ of >2 dB while the values of backscatter STD measured here are ≤1.3 dB). We define "best" and "worst" case scenarios as those providing the radar altimeter the capability of probing respectively the deepest and shallowest sea depths. Our best-case scenario would be represented by a seafloor with the highest possible dielectric contrast (i.e., the lowest relative permittivity of the liquid found at Punga Mare, or 1.65, and a high seafloor relative permittivity indicating higher order organics, or ammonia, or 5.5) with a very low small-scale roughness (i.e., 1°RMS slope). Conversely, the worst-case scenario could be represented by a very low dielectric contrast (i.e., the less methane-dominated liquid medium similar to the one found at the Ontario lacus, 1.76 of relative permittivity, with a seabed composed of a mix of water ice and solid hydrocarbons, 2.5 of relative permittivity) and a relatively high value of small-scale roughness (i.e., 8°RMS slope). While in the best-case scenario the Cassini radar could have probed the seafloor up to ∼300 m, in the worst-case it would have been able to distinguish seafloor echoes of ∼100 m or shallower. Even integrating the entire group of 94 echoes (basin C) located in the central portion of Kraken Mare (which should increase our sensitivity by an additional 50 m) did not reveal any seafloor echo (same applies for Arnar sinus).

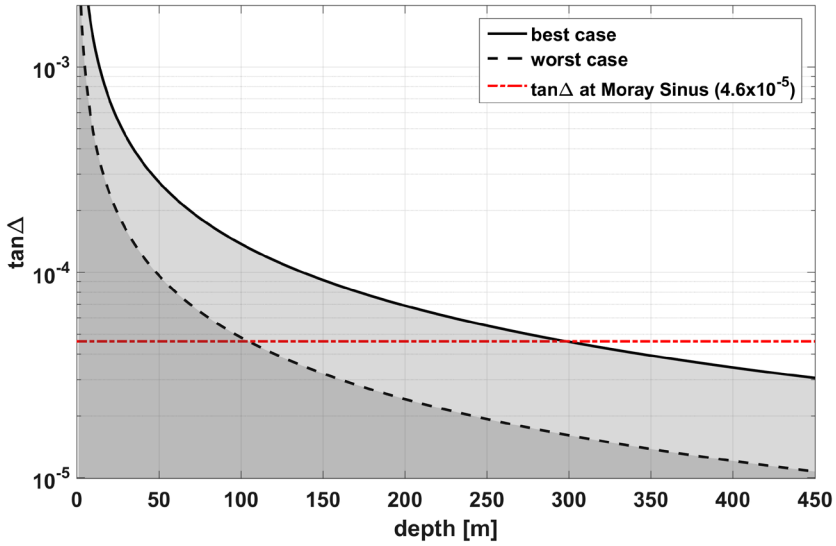

Figure 8. Shaded areas indicate scenarios for which a seafloor echo would have been detected (SNR ≥ 5 dB) by the Cassini radar altimeter in the main body of Kraken Mare in both the seafloor best case ($\varepsilon_s = 1.65$, $\varepsilon_{ss} = 5.5$, seafloor RMS slope = 1°) and worst case ($\varepsilon_s = 1.76$, $\varepsilon_{ss} = 2.5$, seafloor RMS slope = 8°) conditions. RMS, root mean square; SNR, signal-to-noise ratio.

On the other hand, the lack of positive correlation between measured depth and emissivity at Moray Sinus, and the uncertainties in the liquid composition and roughness/permittivity of the sea surface and floor in the main body of Kraken Mare prevent any unambiguous interpretation of the variations in emissivity recorded therein (on average ~0.974 for Arnar Sinus, ~0.967 for basin C, and ~0.964 in Moray Sinus). Once emissivity saturation is reached, that is, the sea bottom is too deep to contribute to the measured microwave thermal emission, variations in nadir emissivity simply reflect slight changes in sea surface small scale roughness, and/or in the liquid permittivity (Le Gall et al., 2016). In this regard, we note that the slightly higher emissivity recorded at the central portions of Kraken (basins B and C) could be ascribed to lower values of permittivity of the liquid and/or a higher small-scale roughness of the sea surface. Using the theoretical model described by Le Gall et al. (2016) (their Equations 6 and 7) and considering a smooth seafloor, in the best-case scenario (with the higher dielectric contrast at the seafloor as described before) the radiometer should be able to sense a seafloor signal up to ~150 m of depth. Conversely, in the worst-case (the lower dielectric contrast at the seafloor as described before) a depth of ~100 m would be again the most likely limit. In this regard, we also note that the sea-surface roughness has little influence on determining the depth at which the emissivity reaches saturation. Thus, if we assume that the same low-loss methane-dominated sea composition observed at Moray Sinus is also present in central Kraken Mare, the observed data suggest sea depth of at least 100–300 m, in the worst and best cases respectively (see Figure 8 for a summary of the admissible scenarios for the main body of Kraken Mare). However, the fact that the emissivity is increasing from Moray to Arnar might argue that saturation has not quite been reached in central Kraken, rendering the depth limit based on radiometry very uncertain. Any future mission to Titan aimed at providing the bathymetry and composition of Kraken Mare should be designed to take advantage of the higher penetration capabilities of lower frequencies, i.e., X-band (Mastrogiuseppe, 2019a).

5. Discussion

Several waveforms acquired over Moray Sinus show the presence of an echo coming from the seafloor. Our simulations indicate that Moray Sinus has a maximum estimated depth along the T104 altimetric track of 85^{+28}_{-18} m and that the specific attenuation of the liquid is 17^{+3}_{-3} dB / μs, corresponding to a loss tangent of $4.6^{+0.9}_{-0.9} \times 10^{-5}$, which is very similar to the loss tangent determined at Ligeia Mare $\left(4.4^{+0.9}_{-0.9} \times 10^{-5}\right)$.

Lorenz (2014) produced a hydrological model to describe the composition of Titan's seas, assuming they are held away from local thermodynamic equilibrium with the atmosphere by the latitudinal variation of precipitation and evaporation. In his model the presence of methane-nitrogen rain increases with increasing latitude, causing the composition of the more poleward seas to be more methane-rich. Noting that Ligeia Mare is directly connected to Kraken Mare by a labyrinth of narrow channels, Lorenz (2014) predicts an evaporation rate of ∼23.6 meters per thousand years, leading to a strong compositional contrast. Comparing the net flow of liquid driven southward from Ligeia to Kraken with the mixing flows driven by tides (see also Vincent et al., 2018) suggests in the Lorenz (2014) model that the composition of Ligeia Mare should be more methane- (and hence nitrogen-)rich than Kraken, with the latter containing a higher fraction of microwave-absorbing ethane. While past measurements (Mastrogiuseppe et al., 2016) confirmed the high values of methane and nitrogen in Ligeia Mare (∼88%), the composition estimated herein for Moray Sinus indicates that, at least in the northernmost area of Kraken Mare where these two seas possibly connect (Figure S3), the amount of ethane is similar to that of Ligeia Mare (see also Table 2). This result does not exclude the possibility of having higher concentrations of ethane further south in Kraken Mare, nor that additional hydrocarbon components in the seas might be providing some of the absorption—although what those might be remains uncertain. Photochemical models of the production of hydrocarbons from methane and Cassini observations (Hörst, 2017) suggest that anything other than ethane would be insufficiently abundant to measurably affect the dielectric constant of the seas.

It is also interesting to note that the average nadir backscatter at Moray Sinus is 8–9 dB lower than Ligeia Mare (see Table 1). Limiting our consideration only to mixtures of CH_4, N_2, and C_2H_6, this difference cannot be explained only by liquid permittivity variations due to varying quantities of the three components. Two end-member scenarios are thus possible: first, a deposition on the liquid surface of one of the two seas of a layer of material with a different effective dielectric constant than the one found at the other sea; second, an enhancement of effective surface roughness on Moray Sinus, caused alternatively by a sea surface that could be broken up by capillary-gravity waves (A. G. Hayes et al., 2013) or perhaps even transient nitrogen bubbles (Cordier et al., 2017).

In the first scenario, we consider the possibility that the surface of the two seas has the same roughness but different effective relative dielectric constants (but with at least one of the two having the expected value of sea surface permittivity of $\varepsilon_s = 1.7$). We then have two possibilities: the surface of Moray Sinus is covered by a material with a very low dielectric constant or Ligeia Mare is covered by a layer with a very high dielectric constant. If no roughness is present on the two seas, then in order to match the available data Moray Sinus has to be covered by a layer with an effective dielectric constant as low as 1.2 ± 0.03. If, instead, the two seas have both a surface roughness of 2.4 mm, then while the southern part of Ligeia Mare must be covered by a material with effective dielectric constant of 4.1 ± 0.3, the northern part requires one with 3.4 ± 0.4. In the first scenario, the surface layer would require a diffuse bottom interface with the liquid in order to not generate constructive/destructive intralayer multiple bouncing, which would cause the sea-surface backscatter to show strong local variations which are not observed (STD of $\sigma_0 \leq \sim 1$ dB). Note that a widespread but time-dependent graded-density surface covering Moray Sinus could also explain the up to ∼11 dB variation of the backscatter observed between the T25 and T28 SAR observations of the area (see Figure 2 and [A. G. Hayes et al., 2011]). Whether the source of this occasional deposit is atmospheric, fluvially injected or from the surrounding terrain is not constrained by the data.

Note also that this scenario would be consistent with the Huygens penetrometer measurements, reported by Atkinson et al. (2010), indicating that the first contact with the surface was into a ∼7 mm thick coating on the substrate material characterized by weaker mechanical properties than terrestrial snow, probably a loose covering of deposited atmospheric aerosols and tholins. Terrestrial snow can show values of permittivity down to 1.4 because of its very high porosity (Ulaby et al., 1986). While the deposits on Titan would not be snow composed of water ice, the mechanical properties leading to high porosity might be analogous. The hypothesis that a lower effective dielectric constant material covered Moray Sinus at the time of the observation is attractive for three reasons. First, because the area already showed signs of variability in the T25/T28 observations. Second, emissivity of the northern Ligeia mare and Moray sinus are similar at ∼50 m of depth (∼0.964 within the 1% accuracy, see Figure 6, panels d and f). While a

difference in sea surface roughness would correspond to an appreciable difference in emissivity (i.e., an increase from 0 to 2.4 mm of RMS height would cause an increase of ≥0.3% in emissivity), the presence of a thin or, perhaps more likely, spatially varying subfootprint layer of deposits (eventually with different values of effective ε_s for the two seas) would result in a negligible difference in emissivity, like the one we observed between these two liquid bodies. Third, although the densities of solid hydrocarbon and nitrile products at Titan temperatures are larger than that of the liquid, such deposits are porous at either the macroscopic or (in the case of polyacetylene) microscopic level. The porosity of such deposits and the turbulent processes active near the surface of the sea plausibly make them neutrally or even positively buoyant. Wind stress, tidal currents in the presence of topographic obstacles, and/or convection by solar heating would then cause agglomerates of large particles and polymer chains to move upward in the liquid and be maintained in the mixed layer near the surface of the sea (Lunine, 1992).

If instead we ascribe the low values of sea surface backscatter recorded on Moray Sinus to an effect of sea surface roughening (the second scenario), and consider a sea surface permittivity of $\varepsilon_s = 1.7$, we would require an increase of effective sea surface RMS roughness σ_h from the 0.9 ± 0.3 mm of northern Ligeia Mare (see also [Zebker et al., 2014]) to 2.4 ± 0.1 mm in Moray Sinus. Note that nitrogen exsolution in the form of bubbles at the surface of the sea, caused by outflow from methane-nitrogen rivers mixing with more ethane-rich lakes or seas as proposed by Malaska et al. (2017) and Farnsworth et al. (2019), would potentially have two effects: a decrease in the effective permittivity (because of the presence of the empty space within the bubbles themselves), and an increase the effective roughness of the sea surface. Moray Sinus could be such an area.

The variation in the estimated Moray Sinus seafloor permittivity and/or roughness is similar to what has been observed for the seafloor of Ligeia Mare, where the northern half seems to exhibit lower values of permittivity and/or higher footprint-scale roughness with respect to the southern half. In both cases, we expect fluvial networks to be able to discharge large quantities of material close to their termini while the energy of the flow would not be enough to move this material over longer distances. This would cause the seafloor in the deeper portions farther from the coast to appear more compact and flatter to the radar (see Figure 7). Note that the progressive infilling of the seas in the northern polar area, which seems to be occurring on Titan in the present-day (see Aharonson et al. [2009], A. G. Hayes et al. [2011] and Poggiali et al. [2016]), could also have caused the river to discharge its material at progressively smaller distances to the current coastline. This might cause the exposed seafloors located farthest from the coast to be gradually covered by fine sediments and become more compact. On Earth, rivers can deposit coarser sediments near the mouth and finer sediments as one moves seaward, primarily as an effect of tidally driven exchange (for a complete review of the argument see FitzGerald et al. [2012]).

We have constrained sea compositions simultaneously by the microwave absorption using the Lorentz-Lorenz relation, and the solubility data for the ternary methane-ethane-nitrogen mixture. Because laboratory-measured solubilities are temperature dependent (Malaska et al., 2017), we have in principle a consistency check. The volumetric composition that we obtain of 70 (62–77)% CH_4, 16 (14–19)% N_2, and 14 (4–24)% C_2H_6, once converted to mole fraction, is compatible with a temperature between 90 K and 91 K, with the best fit obtained with the lowest ethane solution at a temperature of ∼91 K. This is a reasonable temperature given that the northern seas were gradually warming from vernal equinox, when the T104 altimetric data were acquired in August 2014. In fact, our result is consistent with the radiometric results reported by Le Gall et al. (2016) and the Composite Infrared Spectrometer (CIRS) data reported by Jennings et al. (2016). The latter study, in particular, gives a sea temperature over Ligeia Mare (between 77°N and 83°N) in the period between April 2013 and September 2014 of 91.7 ± 0.8 K. Those results combined with ours lend support to the presence of large-scale methane moisture within the soils of the north polar region delaying the springtime increase in high latitude temperatures (Tokano, 2019).

Despite multiple challenges posed by the unique qualities of the T104 Cassini flyby of Titan, we have constrained the bathymetry and composition of Moray Sinus, as well as investigated its seafloor and sea surface dielectric properties and roughness, thus providing useful constraints on the methane hydrology of the high northern latitudes.

Data Availability Statement

The data that support the findings within this paper are available as Long Burst Data Record products in the NASA Planetary Data System (https://pds-imaging.jpl.nasa.gov/data/cassini/cassini_orbiter) and on the following online repository (https://doi.org/10.35003/SMHEIM). The reader can find in supporting information every additional figure mentioned in the text.

Acknowledgments
The authors would like to express their thanks to the entire Cassini Titan Orbiter Science Team and to the Cassini RADAR Science Team for planning and executing the Kraken Mare inspections reported here: their efforts led to the success of this great mission that will influence planetary science for decades to come. The authors would also like to thank Ralph Lorenz and the other, anonymous, referee for their thoughtful and valuable comments which measurably improved the paper. The authors acknowledge with gratitude the support of Severine Fournier and Brian Dzwonkowski to this research. V. Poggiali, A. G. Hayes acknowledge funding for this work from the NASA CDAP program grant number NNX15AH10 G. J. I. Lunine was supported as a David Baltimore Distinguished Visiting Scientist with contract number 1623526.

References

Aharonson, O., Hayes, A. G., Lunine, J. I., Lorenz, R. D., Allison, M. D., & Elachi, C. (2009). An asymmetric distribution of lakes on Titan as a possible consequence of orbital forcing. *Nature Geoscience*, *2*, 851–854. https://doi.org/10.1038/NGEO698

Alberti, G., Catallo, C., Festa, L., Flamini, E., Orosei, R., et al. (2007). The processing of altimetric data (PAD) system for Cassini RADAR. *Memorie Della Societa Astronomica Italiana*, *11*, 68. https://ui.adsabs.harvard.edu/abs/2007MSAIS..11...68A

Atkinson, K. R., Zarnecki, J. C., Towner, M. C., Ringrose, T. J., Hagermann, A., Ball, A. J., et al. (2010). Penetrometry of granular and moist planetary surface materials: Application to the Huygens landing site on Titan. *Icarus*, *210*, 843–851. https://doi.org/10.1016/j.icarus.2010.07.019

Born, M., & Wolf, E. (1999). *Principles of optics: Electromagnetic theory of propagation, interference and diffraction of light* (7th ed.). Cambridge, UK: Cambridge University Press. https://doi.org/10.1017/CBO9781139644181

Cordier, D., García-Sánchez, F., Justo-García, D. N., & Liger-Belair, G. (2017). Bubble streams in Titan's seas as a product of liquid N_2 + CH_4 + C_2H_6 cryogenic mixture. *Nature Astronomy*, *1*, 0102. https://doi.org/10.1038/s41550-017-0102

Elachi, C., Allison, M. D., Borgarelli, L., Encrenaz, P., Im, E., Janssen, M. A., et al. (2004). Radar: The Cassini titan radar mapper. *Space Science Reviews*, *115*, 71–110. https://doi/org/10.1007/1-4020-3874-7_2

Farnsworth, K. K., Chevrier, V. F., Steckloff, J. K., Laxton, D., Singh, S., Soto, A., & Soderblom, J. M. (2019). Nitrogen exsolution and bubble formation in Titan's lakes. *Geophysical Research Letters*, *46*, 13658–13667. https://doi.org/10.1029/2019GL084792

FitzGerald, D., Buynevich, I., & Hein, C. (2012). Morphodynamics and facies architecture of tidal inlets and tidal deltas. In R. Davis Jr & R. Dalrymple (Eds.), *Principles of tidal sedimentology* (pp. 301–333). Dordrecht, The Netherlands: Springer. https://doi.org/10.1007/978-94-007-0123-6_12

Fournier, S., Chapron, B., Salisbury, J., Vandemark, D., & Reul, N. (2015). Comparison of spaceborne measurements of Sea Surface Salinity and colored detrital matter in the Amazon plume. *Journal of Geophysical Research: Oceans*, *120*, 3177–3192. https://doi.org/10.1002/2014JC010109

Hayes, A. G. (2016). The lakes and seas of Titan. *Annual Review of Earth and Planetary Sciences*, *44*, 57–83. https://doi.org/10.1146/annurev-earth-060115-012247

Hayes, A., Aharonson, O., Callahan, P., Elachi, C., Gim, Y., Kirk, R., et al. (2008). Hydrocarbon lakes on titan: Distribution and interaction with a porous regolith. *Geophysical Research Letters*, *35*, L09204. https://doi.org/10.1029/2008GL033409

Hayes, A. G., Aharonson, O., Lunine, J. I., Kirk, R. L., Zebker, H. A., Wye, L. C., et al. (2011). Transient surface liquid in Titan's polar regions from Cassini, *Icarus*, *211*(1), 655–667. https://doi.org/10.1016/j.icarus.2010.08.017

Hayes, A. G., Birch, S. P. D., Dietrich, W. E., Howard, A. D., Kirk, R. L., Poggiali, V., et al. (2017). Topographic constraints on the evolution and connectivity of Titan's lacustrine basins. *Geophysical Research Letters*, *44*, 11745–11753. https://doi.org/10.1002/2017GL075468

Hayes, A. G., Lorenz, R. D., Donelan, M. A., Manga, M., Lunine, J. I., Schneider, T., et al. (2013). Wind driven capillary-gravity waves on Titan's lakes: Hard to detect or non-existent? *Icarus*, *225*(1), 403–412. https://doi.org/10.1016/j.icarus.2013.04.004

Hayes, A. G., Lorenz, R. D., & Lunine, J. I. (2018b). A post Cassini view of Titan's methane-based hydrologic cycle. *Nature Geoscience*, *11*, 306–313. https://doi.org/10.1038/s41561-018-0103-y

Hayes, A. G., Michaelides, R. J., Turtle, E. P., Barnes, J. W., Soderblom, J. M., Mastrogiuseppe, M., et al. (2014). *The distribution and volume of Titan's hydrocarbon lakes and seas*. 45th Lunar and Planetary Science Conference, held 17-21 March, 2014 at The Woodlands, Texas. LPI Contribution No. 1777, p. 2341. Retrieved from https://ui.adsabs.harvard.edu/abs/2014LPI....45.2341H

Hayes, A. G., Soderblom, J. M., Barnes, J. W., Poggiali, V., & Mastrogiuseppe, M. (2018a). Wind, waves, and magic islands at titan's largest sea Kraken Mare, 49th Lunar and Planetary Science Conference 19–23 March, 2018 held at The Woodlands, Texas LPI Contribution No. 2083, id.2065 Retrieved from https://ui.adsabs.harvard.edu/abs/2018LPI....49.2065H

Hayes, A. G., Wolf, A. S., Aharonson, O., Zebker, H., Lorenz, R., Kirk, R. L., et al. (2010). Bathymetry and absorptivity of Titan's Ontario Lacus. *Journal of Geophysical Research*, *115*, E09009. https://doi.org/10.1029/2009JE003557

Hörst, S. M. (2017). Titan's atmosphere and climate. *Journal of Geophysics Research: Planets*, *122*, 432–482. https://doi.org/10.1002/2016JE005240

Janssen, M. A., Le Gall, A., Lopes, R. M., Lorenz, R. D., Malaska, M. J., Hayes, A. G., et al. (2016). Titan's surface at 2.18-cm wavelength imaged by the Cassini RADAR radiometer: Results and interpretations through the first ten years of observation. *Icarus*, *270*, 443. https://doi.org/10.1016/j.icarus.2015.09.027

Janssen, M. A., Lorenz, R. D., West, R., Paganelli, F., Lopes, R. M., Kirk, R. L., et al. (2009). Titan's surface at 2.2-cm wavelength imaged by the Cassini RADAR radiometer: Calibration and first results. *Icarus*, *200*, 222. https://doi.org/10.1016/j.icarus.2008.10.017

Jennings, D. E., Cottini, V., Nixon, C. A., Achterberg, R. K., Flasar, F. M., Kunde, V. G., et al. (2016). Surface temperatures on Titan during northern winter and spring. *The Astrophysical Journal Letters*, *816*, 1. https://doi.org/10.3847/2041-8205/816/1/L17

Le Gall, A., Malaska, M. J., Lorenz, R. D., Janssen, M. A., Tokano, T., Hayes, A. G., et al. (2016). Composition, seasonal change, and bathymetry of Ligeia Mare, Titan, derived from its microwave thermal emission. *Journal of Geophysical Research: Planets*, *121*, 233. https://doi.org/10.1002/2015JE004920

Lorenz, R. D. (2014). The flushing of Ligeia: Composition variations across Titan's seas in a simple hydrological model. *Geophysical Research Letters*, *41*, 5764–5770. https://doi.org/10.1002/2014GL061133

Lunine, J. I. (1992). *Plausible surface models for Titan*. Proceedings Symposium on Titan, Toulouse, France, 9–12 September 1991 ESA SP-338.

Malaska, M. J., Hodyss, R., Lunine, J. I., Hayes, A. G., Hofgartner, J. D., Hollyday, G., & Lorenz, R. D. (2017). Laboratory measurements of nitrogen dissolution in Titan lake fluids. *Icarus*, *289*, 94–105. https://doi.org/10.1016/j.icarus.2017.01.033

Mastrogiuseppe, M., Hayes, A. G., Poggiali, V., Lunine, J. I., Lorenz, R. D., Seu, R., et al. (2018a). Bathymetry and composition of Titan's Ontario Lacus derived from Monte Carlo-based waveform inversion of Cassini RADAR altimetry data. *Icarus*, *300*, 203–209. https://doi.org/10.1016/j.icarus.2017.09.009

Mastrogiuseppe, M., Poggiali, V., Hayes, A. G., Lunine, J. I., Seu, R., Di Achille, G., et al. (2018b). Cassini radar observation of Punga Mare and environs: Bathymetry and composition. *Earth and Planetary Science Letters*, *496*, 89–95. https://doi.org/10.1016/j.epsl.2018.05.033

Mastrogiuseppe, M., Hayes, A., Poggiali, V., Seu, R., Lunine, J., Hofgartner, J., et al. (2016). Radar sounding using the Cassini altimeter: Waveform modeling and Monte Carlo approach for data inversion of observations of Titan's seas. *IEEE Transactions on Geoscience and Remote Sensing*, *54*, 5646–5656. https://doi.org/10.1109/TGRS.2016.2563426

Mastrogiuseppe, M., Poggiali, V., Raguso, M. C., Wall, S., & Elachi, C. (2019a). *Inversion of Cassini radar data: The Liquid contrast method*. 50th Lunar and Planetary Science Conference, held 18-22 March, 2019 at The Woodlands, Texas. LPI Contribution No. 2132, id.3268. Retrieved from https://ui.adsabs.harvard.edu/abs/2019LPI....50.3268M

Mastrogiuseppe, M., Poggiali, V., Hayes, A.G., Lunine, J. I., Seu, R., Mitri, G., & Lorenz, R. D. (2019b). Deep and methane-rich lakes on Titan. *Nature Astronomy*, *3*, 535–542. https://doi.org/10.1038/s41550-019-0714-2

Mastrogiuseppe, M., Poggiali, V., Hayes, A., Lorenz, R., Lunine, J., Picardi, G., et al. (2014). The bathymetry of a Titan sea. *Geophysical Research Letters*, *41*, 1432–1437. https://doi.org/10.1002/2013GL058618

Mitchell, K. L., Barmatz, M. B., Jamieson, C. S., Lorenz, R. D., & Lunine, J. I. (2015). Laboratory measurements of cryogenic liquid alkane microwave absorptivity and implications for the composition of Ligeia Mare, Titan. *Geophysical Research Letter*, *42*, 1340–1345. https://doi.org/10.1002/2014GL059475

Niemann, H. B., Atreya, S. K., Demick, J. E., Gautier, D., Haberman, J. A., Harpold, D. N., et al. (2010). Composition of Titan's lower atmosphere and simple surface volatiles as measured by the Cassini-Huygens probe gas chromatograph mass spectrometer experiment. *Journal of Geophysical Research*, *115*, E12006. https://doi.org/10.1029/2010JE003659

Picardi, G., Biccari, D., Cartacci, M., Cicchetti, K. A., Giuppi, S., Marini, A., et al. (2008). *MARSIS data inversion approach: Preliminary results*. 2008 IEEE Radar Conference, Rome, pp. 1–4. https://doi.org/10.1109/RADAR.2008.4721073

Poggiali, V., Mastrogiuseppe, M., & Hayes, A. G. (2019). High-resolution topography of titan adapting the delay/Doppler algorithm to the Cassini RADAR altimeter data. *IEEE Transactions on Geoscience and Remote Sensing*, *57*(9), 7262–7268. https://doi.org/10.1109/TGRS.2019.2912575

Poggiali, V., Mastrogiuseppe, M., Hayes, A. G., Seu, R., Birch, S. P. D., Lorenz, R., et al. (2016). Liquid-filled canyons on Titan, *Geophysical Research Letter*, *43*, 7887–7894. https://doi.org/10.1002/2016GL069679

Raguso, M. C., Piazzo, L., Mastrogiuseppe, M., Seu, R., & Orosei, R. (2018). *Resolution Enhancement and Interference Suppression for Planetary Radar Sounders*. 26th European Signal Processing Conference (EUSIPCO), Rome, pp. 1212-1216. https://doi.org/10.23919/EUSIPCO.2018.8553468

Stiles, B. W., Gim, Y., Hamilton, G., Hensley, S., Johnson, W. T. K., Shimada, J., et al. (2006). 2006 IEEE Conference on Radar, Verona, NY, p. 8. https://doi.org/10.1109/RADAR.2006.1631767

Stofan, E. R., Elachi, C., Lunine, J. I., Lorenz, R. D., Stiles, B., Mitchell, K. L., et al. (2007). The lakes of Titan. *Nature*, *445*, 61. https://doi.org/10.1038/nature05438

Thompson, W. R., Squyres, & Steven, W. (1990). Titan and other icy satellites: Dielectric properties of constituent materials and implications for radar sounding. *Icarus*, *86*(2), 336–354. https://doi.org/10.1016/0019-1035(90)90224-W

Tokano, T. (2019). Orbitally and geographically caused seasonal asymmetry in Titan's tropospheric climate and its implication for the lake distribution. *Icarus*, *317*, 337–353. https://doi.org/10.1016/j.icarus.2018.07.025

Ulaby, F. T., Moore, R. K., & Fung, A. K. (1982). *Microwave remote sensing: Active and passive, volume II, radar remote sensing and surface scattering and emission theory*. Reading, MA: Addison–Wesley.

Vincent, D., Karatekin, Ö., Lambrechts, J., Lorenz, R. D., Dehant, V., & Deleersnijder, É. (2018). A numerical study of tides in Titan′s northern seas, Kraken and Ligeia Maria. *Icarus*, 310, 105–126. https://doi.org/10.1016/j.icarus.2017.12.018

West, R. D., Anderson, Y., Boehmer, R., Borgarelli, L., Callahan, P., Elachi, C., et al. (2009). Cassini RADAR sequence planning and instrument performance. *IEEE Transactions on Geoscience and Remote Sensing*, *47*(6), 1777–1795. https://doi.org/10.1109/TGRS.2008.2007217

Wye, L., Zebker, H. A., & Cassini Radar Team. (2011). *Backscatter analysis of Saturn's icy moons with Cassini RADAR*. American Geophysical Union, Fall Meeting 2011, abstract id.P11E-1624. Retrieved from https://ui.adsabs.harvard.edu/abs/2011AGUFM.P11E1624W/abstract

Wye L. C., Zebker H. A., & Lorenz R. D. (2009). Smoothness of Titan's Ontario Lacus: Constraints from Cassini RADAR specular reflection data. *Geophysical Research Letters, 36*(16). https://doi.org/10.1029/2009gl039588

Zebker, H. A., Gim, Y., Callahan, P., Hensley, S., Lorenz, R. & Cassini Radar Team (2009). Analysis and interpretation of Cassini Titan radar altimeter echoes. *Icarus*, *200*, 240. https://doi.org/10.1016/j.icarus.2008.10.023